





# Efficient Hyperspectral Target Detection and Identification With Large Spectral Libraries

Cooper Loughlin , Michael Pieper , Dimitris Manolakis , Randall Bostick, Andrew Weisner , and Thomas Cooley

**Abstract**—Numerous hyperspectral algorithms have been developed to detect both full and subpixel solid target materials. Target signatures are obtained from spectral libraries that contain both target and nontarget materials. When the library is large and contains many potential targets, it is inefficient to run an individual detector for each material of interest. Additionally, such an approach produces numerous false alarms (i.e., multiple detections per pixel) due to spectral similarity among targets. In this article, we present an efficient approach for detecting multiple targets within large spectral libraries while mitigating false alarms. We first group spectrally similar materials within the library into a hierarchy of clusters. From each cluster containing a target material, a single detector is obtained. Each detector represents multiple library spectra, so an identification step is needed for detected pixels. Detected pixels are modeled as a mixture between their local in-scene background and candidate library spectra. Candidates are chosen from adjacent library clusters. The candidate model providing the best fit is chosen to report. Use of local background spectra provides a physically meaningful mixing model that adapts to detected pixels. Clustering the library reduces the computational complexity of modeling detected pixels. We demonstrate detection and false alarm mitigation performance of our proposed algorithm with a real hyperspectral dataset.

**Index Terms**—Adaptation models, computational modeling, detectors, hyperspectral imaging, libraries, mathematical model.

## I. INTRODUCTION

REMOTE detection and identification of solid targets has numerous applications across many disciplines. Hyperspectral imaging (HSI) sensors are well suited for the task due to their high spectral resolution. Hyperspectral detection algorithms compare the spectra of image pixels with target signature spectra and produce a detection score. Target signatures are obtained from a spectral library, which may contain tens of thousands of material spectra. Depending on the application,

materials in a library may be of interest (targets) or not (nontargets). Additionally, libraries may contain multiple signatures for a single material, representing various illumination conditions, intimate mixtures, or other material variability. In this article, we propose an efficient technique for detecting multiple materials in remotely collected hyperspectral imagery using signatures from large spectral libraries.

For multiple targets, the simplest approach is to run an individual detector for each target material signature of interest in the library. This approach has two significant disadvantages. First, when the number of materials is large, the computational cost will be high. Second, and more importantly, numerous false alarms will result. Specifically, multiple detections per pixel are likely to occur for spectrally similar target materials. We consider false alarms to be any detected pixel that does not actually contain the target material of interest. False alarms may also originate from nontarget materials in the scene that are spectrally similar to target materials. An identification (ID) step is needed when detecting multiple targets from a library.

The matched filter (MF) and normalized matched filter (NMF) detectors have been highly successful in practical HSI detection [1]. The NMF is particularly well suited for subpixel targets [2]; however, it exhibits a large number of false alarms [3]. More recently, kernel-based methods [4] and clairvoyant fusion [5] have been proposed for target detection, but their use in practice is less established. Techniques for false alarm mitigation (FAM) have been proposed that exploit MF and NMF geometry [6], [7]. These techniques are able to separate many false alarms, but they do not take advantage of spectral libraries to identify false alarms caused by spectrally similar nontarget materials. Target ID has been addressed using the techniques such as linear unmixing [8], Bayesian model averaging [9], and band selection techniques [10]. Current techniques do not address the challenges posed by large spectral libraries. Specifically, searching the entire library for potential target and background components is inefficient.

The primary motivation of this article is to develop a detection and ID processing pipeline that efficiently leverages large spectral libraries for detection, identification, and FAM. The approach consists of two major components. First, we group spectrally similar materials into a hierarchy of clusters, including both targets and nontargets. To reduce both the number of detectors and multiple detections per pixel, a single detector is obtained for each cluster containing a target of interest. This detector is tuned to a single proxy spectrum, chosen from within

Manuscript received May 18, 2020; revised June 26, 2020 and September 8, 2020; accepted September 21, 2020. Date of publication September 28, 2020; date of current version October 14, 2020. This work was sponsored by the Department of the Air Force under Air Force contract FA8721-05-C-0002. (Corresponding author: Cooper Loughlin.)

Cooper Loughlin, Randall Bostick, Andrew Weisner, and Thomas Cooley are with the Department of Electrical and Computer Engineering, Northeastern University, Boston, MA 02115 USA (e-mail: loughlin.c@husky.neu.edu; andrew.weisner@us.af.mil; randall.bostick@us.af.mil; thomas.cooley@kirtland.af.mil).

Michael Pieper and Dimitris Manolakis are with MIT Lincoln Laboratory, Lexington, MA 02420 USA (e-mail: mpieper@ll.mit.edu; dmanolakis@ll.mit.edu).

Digital Object Identifier 10.1109/JSTARS.2020.3027155

the cluster. Cluster detectors should detect pixels containing any of the materials within the cluster. Since each detector represents multiple spectra, an additional ID/FAM step is taken to identify which specific material is present in a detected pixel.

The goal of identification/false alarm mitigation (ID/FAM) is to determine which, if any, library material is present in the pixel. Pixels may contain target or nontarget materials from the library as well as contributions from spatially adjacent nontarget (background) materials within the scene. Our ID/FAM processing consists of estimating the contribution from library and local background materials for detected pixels. We consider local backgrounds because they are likely present in mixed pixels and it eliminates the need to choose them from the library. They may also account for specific materials or material variability not present in the library. We proceed by modeling each detected pixel as a linear mixture between its local background and candidate library spectra, and then choose the best model. Candidate library spectra are chosen from clusters close to the proxy spectra, as opposed to the entire library. A major contribution of this article is that we model each pixel with both target and nontarget materials from the library. As a result, both ID and FAM are automated. Additionally, hierarchically clustering the library significantly reduces the number of candidate spectra considered to ID each detected pixel, reducing the computational complexity. The novel contributions of our proposed approach can be summarized as 1) combining ID/FAM by leveraging a large spectral library and 2) structuring the library for efficient ID/FAM.

The remainder of the article is organized as follows. Section II provides a brief introduction to hyperspectral target detection. A description of library clustering and detector design is given in Section III. Our proposed ID/FAM processing is described in Section IV. Results for a real hyperspectral cube are presented in Section V and concluding remarks are provided in Section VI.

## II. HYPERSPECTRAL TARGET DETECTION

In hyperspectral target detection, we seek to choose between two mutually exclusive hypotheses, denoted

$$H_0 : \text{target material is absent, or}$$

$$H_1 : \text{target material is present}$$

for each pixel in an image. Pixels without target materials are referred to as background. Reflectance (visible) or emissivity (infrared) spectra are typically used for solid targets, which must be retrieved from measured sensor radiance. Natural variability in surface material spectra, errors in processing algorithms, and sensor noise contribute to random variation in the retrieved spectra. Additionally, mixed pixel spectra will include contributions from each material present. Standard detection algorithms are designed for robustness to these factors.

We can organize the spectra of each pixel into a vector  $\mathbf{x} \in \mathbb{R}^p$ , where  $p$  is the number of spectral bands of the sensor. A detection algorithm designed for a particular target material with library spectrum  $\mathbf{s}$  can be denoted

$$y = D(\mathbf{x}, \mathbf{s}). \quad (1)$$

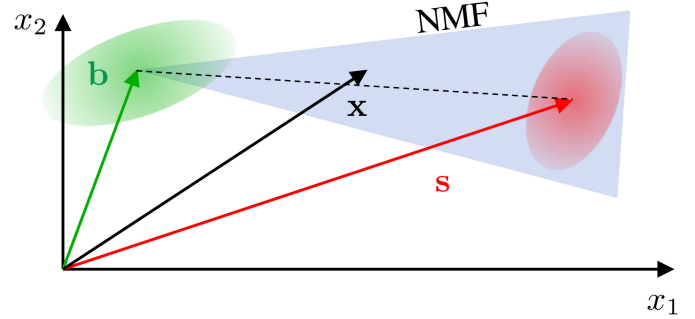


Fig. 1. NMF detection surface is a cone extending from the background spectrum. Subpixel targets lie along the simplex (dashed line) defined by the target and background spectra. Pixel spectrum  $\mathbf{x}$  is shown for some  $0 < a_t < 1$ .

The mixed pixel spectrum for solid subpixel targets includes contributions from both the target and background materials. The contributions are proportional to their pixel fill-fraction. Assuming a mixture of one target and one background, the input spectrum can be modeled

$$\mathbf{x} = a_t \mathbf{s} + (1 - a_t) \mathbf{b} + \mathbf{n} \quad (2)$$

where  $\mathbf{b}$  is the background spectrum and  $\mathbf{n}$  is a term that accounts for variability. The scalar  $a_t$  corresponds to target fill-fraction and is restricted on the interval  $0 \leq a_t \leq 1$ . When  $a_t = 1$ , the target occupies the full pixel. (2) is referred to as the target replacement model. Based on (2), the two hypotheses can be denoted

$$H_0 : a_t = 0 \quad (3a)$$

$$H_1 : a_t > 0. \quad (3b)$$

Subpixel target spectra lie along the simplex defined by the tips of the target and background vectors. An example mixed pixel spectrum is shown in black in Fig. 1. As the fill fraction  $a_t$  decreases from 1 to 0, the mixed pixel spectrum traces the line segment between the target and background spectra.

The MF detection algorithm is effective for full-pixel targets. It has been shown that the NMF is effective for subpixel targets. Both detectors have a simple geometric interpretation [2]. If we define the whitened and centered vector  $\tilde{\mathbf{x}} = \mathbf{C}_b^{-1/2}(\mathbf{x} - \boldsymbol{\mu}_b)$ , where  $\boldsymbol{\mu}_b$  and  $\mathbf{C}_b$  are the mean and covariance of the background pixels, the MF and NMF are defined as

$$y_{\text{MF}} = \frac{\tilde{\mathbf{s}}^T \tilde{\mathbf{x}}}{\|\tilde{\mathbf{s}}\|} \quad (4a)$$

$$y_{\text{NMF}} = \frac{\tilde{\mathbf{s}}^T \tilde{\mathbf{x}}}{\|\tilde{\mathbf{s}}\| \|\tilde{\mathbf{x}}\|} \quad (4b)$$

where  $\|\cdot\|$  denotes the  $\ell^2$  norm. Typically,  $\boldsymbol{\mu}_b$  and  $\mathbf{C}_b$  are unknown and must be estimated from data. The MF measures the length of the projection of  $\tilde{\mathbf{x}}$  in the direction of  $\tilde{\mathbf{s}}$ , while the NMF measures the cosine of the angle between  $\tilde{\mathbf{x}}$  and  $\tilde{\mathbf{s}}$ . The NMF geometry is depicted in Fig. 1. The cone-shape detection surface encompasses the mixing simplex, making it effective for subpixel targets. The squared NMF detector is also referred to as the adaptive cosine estimator (ACE). The NMF is the primary detector used in this work.

### III. LIBRARY CLUSTERING

Spectral libraries may be organized into categories and sub-categories based on material descriptions (e.g., man-made, vegetation, minerals, etc.). This classification structure does not reflect spectral similarities among materials. Alternatively, library spectral clustering groups materials by spectral shape. The goal of library clustering is to group materials with high spectral similarity for dual purposes. The first is to group targets that may be detected by a single proxy target signature. The second is to determine nontarget materials that are spectrally similar to targets. These are referred to as confusers. Hierarchical clustering provides a natural framework for clustering library spectra to achieve these goals. In the following section, a brief description of hierarchical clustering will be provided followed by a method for designing detectors from the clustered library.

#### A. Hierarchical Clustering

Hierarchical clustering is a process by which data are partitioned in a hierarchical manner based on a similarity metric. In hierarchical agglomerative clustering (HAC), each data point begins as its own partition and pairs are grouped as the hierarchy ascends stages. At the top stage, all the data belong to a single partition. At each intermediate stage, a new partition is created by linking the two most similar existing partitions. HAC has been applied to hyperspectral images [11]–[14]; however, it has not been applied to spectral libraries for target identification.

The choice of similarity measure between data points plays a significant role in the clustering result. Our goal is to have spectra within the same cluster respond similarly to the NMF; therefore, we use spectral angle defined as

$$\theta_{ij} = \angle(\mathbf{s}_i, \mathbf{s}_j) = \arccos\left(\frac{\mathbf{s}_i^T \mathbf{s}_j}{\|\mathbf{s}_i\| \|\mathbf{s}_j\|}\right). \quad (5)$$

We consider angular distance in this work, rather than euclidean, because spectral shape is relevant to the NMF while relative magnitude is not. The angle between two existing clusters is also needed for HAC. There are a handful of ways to compute this distance generally considered in the literature [15]. In this work, we use the unweighted average distance due to its clear interpretation and empirical performance. The distance between two clusters is computed as the average pairwise angle distance between each of the spectra in the two clusters. We note that in this scheme, the distance between two individual spectra in different clusters may be smaller than the distance between clusters.

HAC is best visualized by a dendrogram. Fig. 2 shows the dendrogram for paint and paint pigment spectra from the United States Geological Survey (USGS) spectral library [16]. Dendrograms consist of links and leaves. Leaves, denoted by vertical lines, represent clusters. At the bottom, clusters correspond to individual spectra. Linkages, represented by horizontal lines, show what partitions are grouped together as the dendrogram is ascended. The height of the linkage corresponds to the distance between the two partitions being linked. The horizontal axis

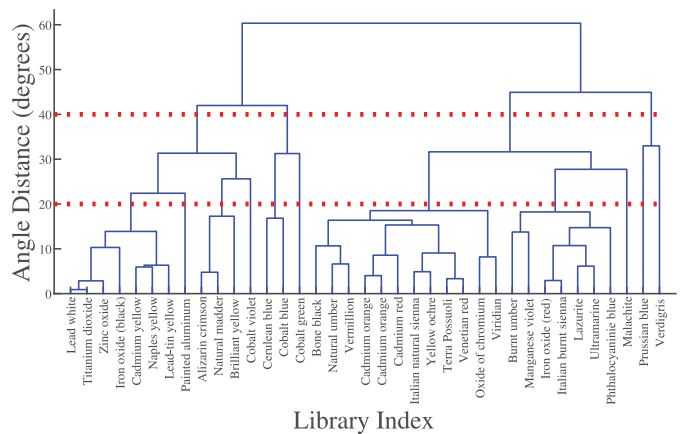


Fig. 2. Dendrogram showing two example distance thresholds (red dotted lines) that determine clustering schemes. The larger threshold (40°) results in 4 clusters while the smaller (20°) results in 11.

corresponds to individual spectra where the order is optimized for visualization.

Clusters can be defined by setting a distance threshold, represented by the red horizontal lines across the dendrogram in Fig. 2. Leaves crossing the cluster threshold correspond to individual clusters, and all spectra descended from those leaves are in the same cluster. Additionally, all the linked leaves within a cluster are said to be adjacent. We can think of adjacent leaves as those that combine into the same cluster as the cluster threshold is raised. A key feature of HAC is that it is based on the series of linkages in the data. Thus, once this series has been computed, different clustering schemes are easily obtained by setting various distance threshold. A large cluster threshold results in few clusters with many leaves in each, while a small threshold results in many clusters with relatively few leaves. For a library of  $N$  signatures, the computational complexity of HAC is  $\mathcal{O}(N^2)$  [17]. The complexity is high; however, the clustering need only be done once for a particular library, and thus does not affect real-time performance.

#### B. Cluster Detectors

We define library clusters by setting a distance threshold in the agglomerative hierarchy, shown as red horizontal lines in Fig. 2. We then obtain NMF detectors for each cluster. There are two competing criteria relevant when selecting a cluster threshold. The first is to reduce the number of detectors, which would suggest a large cluster threshold. The other is to have high similarity within clusters and high dissimilarity between, suggesting a smaller threshold. In this work, a cluster threshold  $\theta_{\text{DET}}$  was chosen experimentally and discussed in Section V-B.

The resulting library clusters may contain only targets, only nontargets, or both. The number of clusters containing at least one target is denoted  $M$ . We therefore need only obtain  $M$  detectors. The cluster detectors are tuned to a single proxy spectrum  $\mathbf{s}_m$  chosen from within the cluster. The proxy is chosen as the target material with the minimum average angle distance to each of the other spectra in the cluster. The result is a bank of  $M$  NMF detectors shown in Fig. 3. Each of the  $N$  pixels in

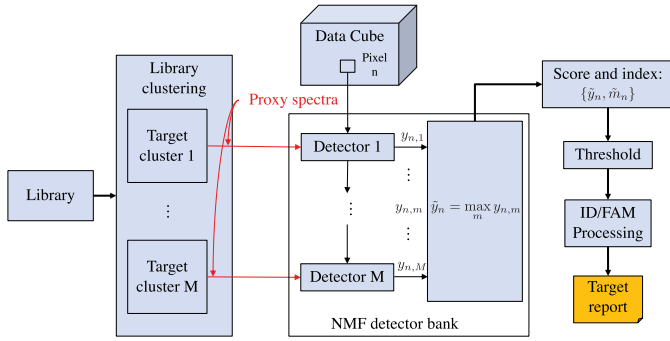


Fig. 3. Each pixel of the data cube is passed through the bank of  $M$  detectors. The maximum score and detector index are chosen, thresholded, and passed to the ID/FAM processing step.

an image is run through the bank of  $M$  detectors, and detection scores are computed for each as  $y_{n,m} = D(\mathbf{x}_n, \mathbf{s}_m)$ , where  $m$  is the cluster index and  $n$  is the pixel index. We choose the maximum score

$$\tilde{y}_n = \max_m y_{n,m} \quad (6)$$

and corresponding detector index  $\tilde{m}_n$  for each pixel. We now have a single score and index for each pixel  $\{\tilde{y}_n, \tilde{m}_n\}_{n=1}^N$ , and we can apply a detection threshold to the scores. The detection threshold should be chosen low enough so that subpixel targets are passed for each signature of interest. If it is assumed the outputs approximately follow a Gaussian distribution, a threshold can be selected for an expected false alarm rate (FAR). A threshold may also be selected using more accurate performance prediction techniques such as [18], [19]. Detected pixels are passed to the ID/FAM step. A block diagram of the detector processing pipeline is shown in Fig. 3.

#### IV. IDENTIFICATION AND FALSE ALARM MITIGATION

Each cluster detector represents multiple spectra from the library. An identification step is essential to report which, if any, material from the library is present in a detected pixel. Because of the spatial resolution of most HSI systems, it is assumed that detected pixels contain at most a single target material. We first group spatially adjacent detected pixels into objects, and then model detected objects as a mixture of local background and candidate library spectra. The estimated target component of each candidate model is compared to the corresponding library signature. Candidate signatures are chosen from clusters adjacent to the detected cluster. The library signature resulting in the best model is selected. If the selected signature is a target, a detection is reported. If a nontarget confuser is selected, the detected pixel is considered a false alarm and not reported. If none of the library spectra provide an adequate model, the object is also not reported. This process automatically mitigates false alarms by determining if pixels are best modeled by target or confuser materials. In the following section, local background and library signature modeling for each detected object will be described.

#### A. Candidate Library Signature Selection

A detected pixel has an associated cluster detector index  $m$  and proxy spectrum  $\mathbf{s}_m$ . Candidate library signatures are chosen based on the detector index  $m$  associated with a detected pixel. If a library material is present in the detected pixel, it is likely similar to the proxy  $\mathbf{s}_m$  and present in cluster  $m$ . However, it is also possible that the true material was mistakenly included in an adjacent library cluster due to material variability. Searching the entire library for candidate spectra is inefficient, since most of the library need not be considered. We can choose candidate library spectra as those belonging to cluster  $m$  as well as adjacent clusters. Adjacent clusters can be determined by setting a new angle threshold  $\theta_{ID}$  on the hierarchy, where  $\theta_{ID} > \theta_{DET}$ . The result is a new set of  $L$  ID clusters, where  $L < M$ . Candidate signatures are chosen from the ID cluster containing the detection cluster  $m$  associated with the current pixel. The cluster threshold  $\theta_{ID}$  should be chosen large enough to account for material variability but small enough to be computationally efficient. This step represents the primary computational savings in our proposed method because it significantly limits the number of candidate signatures considered for each pixel. The exact computational savings depend on the library, designated target signatures, and scene being processed. The choice of  $\theta_{ID}$  and computational savings are discussed in Section V-C.

#### B. Local Background Modeling

Sub-pixel targets are likely to be mixed with the spectra of adjacent background pixels. Background spectra change throughout the image due to variability in materials and illumination. Modeling subpixel targets as a mixture between local in-scene background and library spectra provides a model that is physically meaningful, adaptive to each pixel, and simple to compute. An alternative approach is to use library spectra for the background component of subpixel targets. This would add significant computational complexity, since the correct combination of background and target materials would need to be determined for each pixel. Additionally, library signatures do not reflect background variability throughout the scene.

To obtain local backgrounds, detected pixels are first grouped into detected objects. The target and associated local background pixels for an example target are shown in Fig. 4. Pixels are grouped with their 8-connected neighbors. For each object, the pixel with the maximum score is identified as the primary. Adjacent pixels that do not pass the initial detection threshold may still contain some amount of target material and should not be included in the local background. These guard pixels are identified by masking adjacent pixels with detection scores above a low threshold (e.g., 1 standard deviation). Background pixels are obtained by accumulating nonguard and nondetected pixels within an increasing radius of the primary pixel until a prescribed minimum number of pixels  $K$  is reached. A value of  $K = 18$  was found to work well in practice.

The local background spectra will exhibit some variability; however, it is reasonable to assume they belong to a small number of unique materials that surround each object. The background spectra for the target in Fig. 4 are shown in Fig. 5.

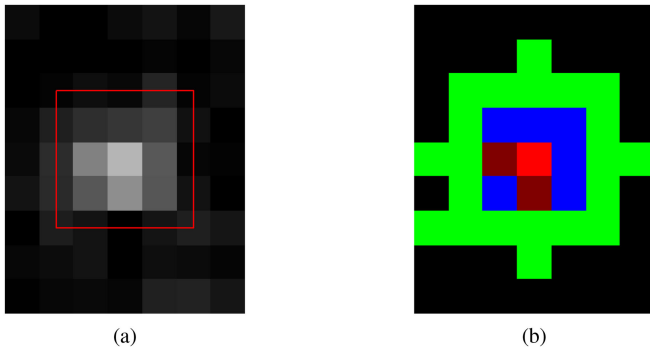


Fig. 4. (a) NMF detection scores are rendered as grayscale values for a particular target, enclosed by the red box. (b) Primary pixel is shown in red, other detected pixels in maroon, local background in green, and guard in blue.

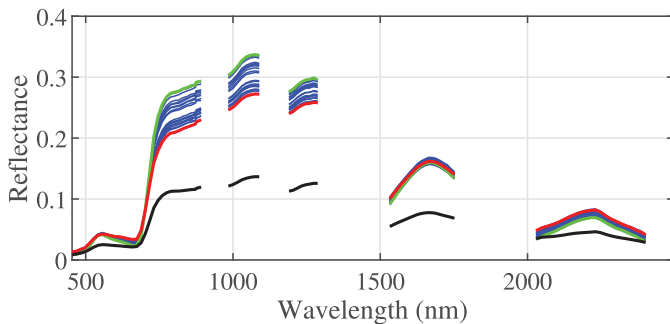


Fig. 5. Local background spectra for the target in Fig. 4 are shown in blue and the subspace basis vectors are in red and green. The shape of the local spectra can be well captured by the basis. The background mean for the entire image is shown in black.

Most of the variability in the background can be captured by a low-dimensional subspace. Given the set of background spectra  $\{\mathbf{b}_1, \dots, \mathbf{b}_k, \dots, \mathbf{b}_K\}$ , the subspace basis vectors  $\mathbf{B} = [\mathbf{b}_k \ \mathbf{b}_{k'}]$  are chosen such that

$$k, k' = \arg \max_{k, k'} \angle(\mathbf{b}_k, \mathbf{b}_{k'}). \quad (7)$$

These two vectors are chosen to capture the variability in the shape of the local background spectra. This is not possible when using library spectra for backgrounds. Additionally, the background mean of the image, shown in black, does not capture the magnitude of the local background for this target.

### C. Library Signature Modeling

Using local background spectra and candidate library signatures, we can estimate a model, denoted  $\hat{\mathbf{x}}$ , for each object's primary pixel spectrum. The modeling technique is similar to that used in [8]. For a particular library spectrum  $\mathbf{s}_i$ , the pixel estimate is of the form

$$\hat{\mathbf{x}}_i = \Phi_i \hat{\mathbf{a}}_i \quad (8)$$

where  $\Phi_i = [\mathbf{s}_i \ \mathbf{B}]$ ,  $\mathbf{B}$  is the local background subspace basis, and  $\mathbf{a}_i = [\hat{a}_{t,i} \ \hat{\mathbf{a}}_{b,i}]$ . The spectrum estimate  $\hat{\mathbf{x}}_i$  is referred to as model  $i$ . If we define the background component of the estimate as  $\hat{\mathbf{b}}_i = \mathbf{B} \hat{\mathbf{a}}_{b,i}$  and the library component as  $\hat{\mathbf{s}}_i = \hat{a}_{t,i} \mathbf{s}_i$ , the pixel

spectrum can be written

$$\mathbf{x} = \hat{\mathbf{s}}_i + \hat{\mathbf{b}}_i + \mathbf{e}_i. \quad (9)$$

The term  $\mathbf{e}_i$  accounts for all sources of error, including sensor noise, spectral variability, and model error. The residual sum of squares (RSS) for the model is defined as

$$\text{RSS}_i = \|\mathbf{e}_i\| = \|\mathbf{x} - \hat{\mathbf{x}}_i\|. \quad (10)$$

We can additionally define the target component as

$$\hat{\mathbf{t}}_i = \mathbf{x} - \hat{\mathbf{b}}_i \quad (11)$$

$$= \hat{\mathbf{s}}_i + \mathbf{e}_i. \quad (12)$$

Model  $i$  is consistent with the data when signature  $\mathbf{s}_i$  is present in pixel  $\mathbf{x}$ . In this case,  $\hat{\mathbf{t}}_i$  should be similar in shape to  $\mathbf{s}_i$  and  $\text{RSS}_i$  should be relatively small.  $\text{RSS}_i$  will be significantly larger when the model is incorrect.

We estimate the model components by minimizing (10). The physics of the target replacement model (2) dictate that the pixel spectrum lies on the simplex defined by the background and target spectrum. When the target and background endmembers are known, this leads to a full constrained least squares (FCLS) problem where  $\sum_j a_j = 1$  (sum-to-one) and  $a_j > 0$  (positivity). In this work, we relax the constraints based on the fact that the background subspace is estimated from the scene and the target component may exhibit mismatch with the library. A major source of spectral variability is illumination, which causes retrieved reflectance spectra to vary in apparent brightness. This manifests as a scaling along the direction of the spectrum. If the sum-to-one constraint is removed, modeled spectra are allowed to lie anywhere in the convex hull defined by the library and background components, allowing for variability in scale. The solution to the resulting non-negative least squares (NNLS) is obtained by iteratively computing the unconstrained LS solution and removing spectra with negative coefficients until all coefficients are positive. At each iteration, negative coefficients are set to zero, so it is possible to have exact zeros in the NNLS solution [20].

### D. Model Decision

Once the detected object has been modeled with each candidate spectrum, it remains to choose the best model. The correctness of the models can be evaluated by measuring the spectral angle between the candidate spectrum and estimated target component of the model,  $\theta_i = \angle(\mathbf{s}_i, \hat{\mathbf{t}}_i)$ . Spectral angle measures only the difference in shape between spectra, not scale. If the library model is correct,  $\theta_i$  should be small, even if their relative scales are different. The angle difference in this case is mostly due to noise. If the library model is incorrect,  $\theta_i$  is mostly due to model mismatch between the library signature and pixel target component estimate. Additionally, angle increases as  $\hat{a}_{t,i}$  decreases, since  $\hat{\mathbf{t}}_i$  would be mostly noise. The best library signature model  $\hat{i}$  is chosen as the one with the smallest angle  $\theta_{\hat{i}}$

$$\hat{i} = \arg \min_i \angle(\mathbf{s}_i, \hat{\mathbf{t}}_i). \quad (13)$$

The resulting model parameters are  $\hat{a}_t = \hat{a}_{t,\hat{i}}$  and  $\hat{\mathbf{a}}_b = \hat{\mathbf{a}}_{b,\hat{i}}$ . Note that since

$$\cos(\theta_{\hat{i}}) = \frac{\mathbf{s}_{\hat{i}}^\top \hat{\mathbf{t}}_{\hat{i}}}{\|\mathbf{s}_{\hat{i}}\| \|\hat{\mathbf{t}}_{\hat{i}}\|} = \frac{\hat{a}_t \mathbf{s}_{\hat{i}}^\top \mathbf{s}_{\hat{i}} + \mathbf{s}_{\hat{i}}^\top \mathbf{e}_{\hat{i}}}{\|\mathbf{s}_{\hat{i}}\| \|\hat{\mathbf{t}}_{\hat{i}}\|} \quad (14)$$

the model angle  $\theta_{\hat{i}} \geq 90$  degrees only when  $\hat{a}_t = 0$ . An alternative approach is to use  $\text{RSS}_{\hat{i}}$  to choose the best model; however,  $\text{RSS}_{\hat{i}}$  is sensitive to the pixel magnitude and may be small even if spectral angle is large or no target material is present. The model  $\text{RSS}_{\hat{i}}$  is, nevertheless, useful for filtering false alarms. For instance, if the  $\text{RSS}$  is large for all of the candidate models, the object is likely a false alarm. An example is discussed in Section V-C.

Once the best library signature has been selected, it remains to determine whether the pixel is best described by the library model or a purely background model. The decision can be formulated as the equivalent hypothesis tests

$$H_0 : \hat{a}_t = 0 \quad \text{or} \quad H_0 : \theta_{\hat{i}} \geq 90 \text{ deg} \quad (15a)$$

$$H_1 : \hat{a}_t > 0 \quad H_1 : \theta_{\hat{i}} < 90 \text{ deg} \quad (15b)$$

where  $H_1$  corresponds to the decision that library signature  $\hat{i}$  is present. The decision  $H_0$  is reached when the NNLS solution includes only local background spectra. Note that since the NNLS algorithm can eliminate elements in the model, it is possible to get exact zeros in the solution. In this case, none of the candidate spectra explain the shape of the pixel spectrum better than the local background spectra. It is possible to obtain values for  $\hat{a}_t$  which are positive but small when the library signature is not actually present. The corresponding angle would be close 90 degrees, indicating the estimated target component is approximately orthogonal to the library signature. False alarms of this type can be further removed by setting a threshold on the model angle and are discussed in Section V-C.

## V. RESULTS

In this section, results of the proposed ID/FAM algorithm are presented. Results were generated using a readily available hyperspectral data set and spectral library. Initial detection results using the NMF are presented and an appropriate initial threshold is selected. After setting an initial detection threshold, ID/FAM results are computed for various  $\theta_{\text{ID}}$ . It is shown that using our technique, high-scoring false alarms can be automatically removed while detecting subpixel targets.

### A. Description of Data

1) *Image Data*: For this work, we use data collected around Cooke City, MT as part of a field experiment from July 2006 [21]. The data was chosen because it has targets with ground truth reflectance spectra. The data was collected by the HyMap sensor, which has 126 bands spanning wavelengths 450 – 2,500 nm. After removing atmospheric absorption bands, 88 remain. The ground resolution of the image is approximately 3 m.

The original Cooke City data has vehicle and fabric targets with ground truth locations. The data was collected over a populated area, so there are numerous objects in the scene with



Fig. 6. An RGB rendering of a section of the Cooke City, MT hyperspectral cube where the section used is in the red box.

TABLE I  
PAIRWISE ANGLE DISTANCES BETWEEN THE TARGET SIGNATURES,  
SHOWN IN DEGREES

|    | F1 | F2   | F3   | F4   |
|----|----|------|------|------|
| F1 | 0  | 19.1 | 23.1 | 4.4  |
| F2 |    | 0    | 26.3 | 17.4 |
| F3 |    |      | 0    | 23.3 |
| F4 |    |      |      | 0    |

no ground truth, including other vehicles and fabrics. Since we do not have ground truth, these objects would be considered false alarms even if they are in fact correctly identified. As a remedy, we illustrate the FAM performance of our method on a  $400 \times 280$  (112 000 total) pixel section of the image that omits the city and includes only the fabric targets. An RGB rendering of the hyperspectral cube is shown in Fig. 6, with the section used boxed in red. Four fabric materials, denoted F1 (red cotton), F2 (yellow nylon), F3 (blue cotton), and F4 (red nylon), are present in the image. Materials F3 and F4 have two locations each of different sizes, denoted a and b. The targets are summarized in Table II. Targets F3 and F4 are less than 3 m, so both are subpixel.

2) *Library*: We use the USGS spectral library in this work [16]. The library contains  $N = 1552$  reflectance spectra for artificial and naturally occurring materials. A version of the USGS library has been sampled to the HyMap sensor resolution. We embedded the 11 Cooke City ground truth target signatures in the library prior to clustering. The USGS library is relatively small compared to what might be found in practice; however, it is used here for illustration purposes because it is readily available.

Fig. 7(a) shows the dendrogram of the USGS library with the fabric target signatures embedded and Fig. 7(b) shows the number of clusters as the angle threshold varies. The total number of clusters (left axis) drops quickly as the angle increases. The right axis shows the number of mixed clusters, defined as those containing both targets and nontargets. At distance thresholds less than 2.6 degrees, each target signature is in its own cluster. The targets combine with nontarget clusters until a maximum is reached at 9.8 degrees, after which the number decreases. At the highest threshold, all the signatures are in one cluster. Fig. 7(c) shows the total number of signatures in the mixed clusters versus  $\theta_{\text{ID}}$ . The large jumps show where large clusters combine.

As  $\theta_{\text{ID}}$  is increased, we should expect the FAR to decrease, as false alarms are identified as nontargets from the library. As more clusters are combined, the computational cost increases. This suggests an optimal range for the ID threshold where a substantial number of candidate signatures are considered, but

TABLE II  
IDENTIFICATION RESULTS FOR TARGETS IN THE SCENE

| $\theta_{ID}$ (deg) | FAR                   | # of ID Signatures | Targets                   |                                     |                             |                             |                            |                           |
|---------------------|-----------------------|--------------------|---------------------------|-------------------------------------|-----------------------------|-----------------------------|----------------------------|---------------------------|
|                     |                       |                    | F1:<br>Red Cotton<br>(3m) | F2:<br>Yellow Nylon<br>(3m)         | F3a:<br>Blue Cotton<br>(1m) | F3b:<br>Blue Cotton<br>(2m) | F4a:<br>Red Nylon<br>(1m)  | F4b:<br>Red Nylon<br>(2m) |
| 2.6                 | $3.05 \times 10^{-3}$ | 5                  | <b>F1</b>                 | <b>F2</b>                           | <b>F3</b>                   | <b>F3</b>                   | <b>F4</b>                  | <b>F4</b>                 |
| 8.5                 | $1.68 \times 10^{-3}$ | 8                  | <b>F1</b>                 | <b>F2</b>                           | <b>F3</b>                   | <b>F3</b>                   | Red Nylon                  | Red Nylon                 |
| 9.8                 | $9.26 \times 10^{-4}$ | 161                | <b>F1</b>                 | Gypsum, jarosite,<br>Illite mixture | <b>F3</b>                   | <b>F3</b>                   | Red Nylon                  | Red Nylon                 |
| 17.4                | $9.99 \times 10^{-5}$ | 955                | <b>F1</b>                 | Perennial grass                     | Green Cotton                | Viridian Paint              | Wetland Perennial<br>Grass | Potassium<br>ferrocyanide |
| 23.0                | $9.99 \times 10^{-5}$ | 1060               | <b>F1</b>                 | Perennial grass                     | Green Cotton                | Viridian Paint              | Wetland Perennial<br>Grass | Potassium<br>ferrocyanide |
| 40.6                | $9.99 \times 10^{-5}$ | 1563               | <b>F1</b>                 | Oiled Marsh Plant                   | Cedar Shake                 | Cedar Shake                 | Wetland Rush               | Cedar Shake               |

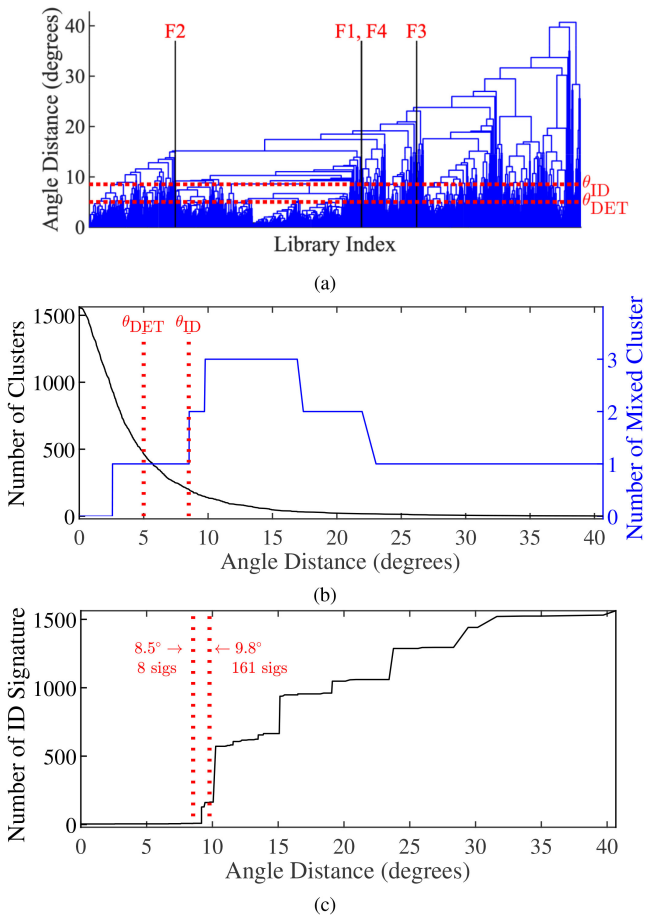


Fig. 7. (a) Dendrogram for the full USGS spectral library with the fabric target signatures (red) embedded. (b) The left vertical axis shows the total number of library clusters as the angle threshold increases. The right axis shows the number of clusters containing both target and nontarget signatures. The angle threshold for detection and ID/FAM with the best results are also shown. (c) The number of candidate signatures being considered is shown versus  $\theta_{ID}$ .

the number of mixed clusters is not saturated. From Fig. 7, this corresponds to an ID threshold range of 8.5–9.8 degrees.

### B. Initial Detection Results

As the first step in the ID/FAM processing, we run an NMF detector for each of the proxy spectra. The pairwise angle

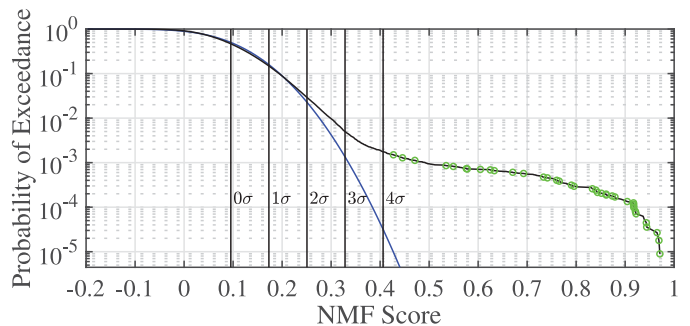


Fig. 8. Probability of exceedance for the maximum NMF scores are shown with the ground truth pixels shown in green. Probability of exceedance is shown in blue for a Gaussian distribution with the mean and standard deviation of the maximum pixel NMF scores.

distances between the target spectra are shown in Table I. The target signatures are significantly different from each other, with the exception of F1 (red cotton) and F4 (red nylon), which are less than 5 degrees apart. For these targets, material color affects the angle similarity more than the fabric type. To demonstrate the use of proxy spectra, we can set  $\theta_{DET} = 5$  degrees. The resulting proxy spectra are F1, F2, and F3.

The probability of exceedance versus detection threshold for the maximum NMF scores  $\tilde{y}_n$  is shown in Fig. 8. Also shown are various thresholds based on the standard deviation of the scores  $\sigma = \sqrt{\text{Var}(\tilde{y}_n)}$ . The vertical lines correspond to the specified number of standard deviations above the mean. The green markers are the maximum scores of the target pixels in the scene. A threshold of at most  $4\sigma$  should be used to capture all 38 of the target pixels. In real applications, however, the target information is not known and a threshold must be selected in a systematic way. If it is assumed the outputs approximately follow a Gaussian distribution, a threshold can be selected for an expected FAR. A threshold of  $3\sigma$  results in an expected FAR of  $1.3 \times 10^{-3}$  while passing even the smallest targets. The  $3\sigma$  NMF score is  $y_{NMF} \approx 0.33$ , which corresponds to a maximum 70 degrees of angle difference between the target and test pixel in the whitened space. This suggests that with such a low detection threshold, the dendrogram threshold  $\theta_{DET}$  actually has little effect on the ability to detect targets and can be set primarily to limit computation. Using this threshold, 556 pixels

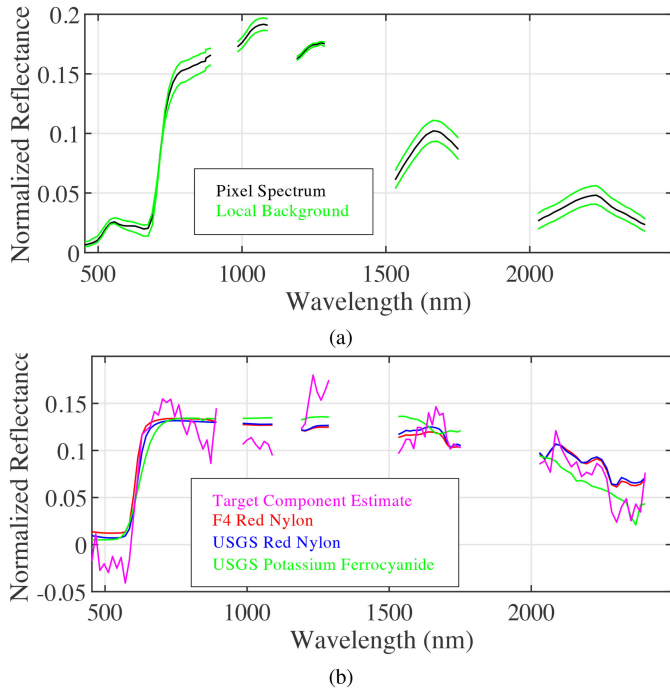


Fig. 9. (a) Normalized pixel and local background subspace spectra are shown. The pixel spectrum strongly resembles the local background. (b) Target and identified library spectra are shown as well as the estimated target component. There is clear similarity among the target and library spectra. The estimated target component shares a similar shape but with residual modeling error.

are detected, 518 of which are false alarms, based on the Cooke City ground truth. All 38 target pixels are detected with a FAR of  $3.05 \times 10^{-3}$ . The detected pixels are grouped into 188 objects after local background modeling.

### C. Identification and False Alarm Mitigation

In this section, we present the ID/FAM results for the Cooke City, MT data. We analyze the effect of library clustering and threshold selection on the ID/FAM performance by varying  $\theta_{ID}$  and computing results, which are compiled in Table II. The  $\theta_{ID}$  values are those where the number of mixed clusters changes, taken from Fig. 7(b).

At  $\theta_{ID} = 2.6$  degrees, each of the targets is correctly identified with their true signatures; however, the FAR is high. This is to be expected, since at that threshold, each of the target signatures is in their own cluster. As  $\theta_{ID}$  is further increased, the FAR is reduced while targets tend to be misidentified. The reduction in false alarms is due to modeling detected objects and removing those best described by nontarget library materials. At  $\theta_{ID} = 8.5$ , we have a FAR of  $1.68 \times 10^{-3}$  with all targets correctly identified. This is reduced from  $3.05 \times 10^{-3}$  at  $\theta_{ID} = 2.6$ . At  $\theta_{ID} = 9.8$ , the FAR is further reduced to  $9.26 \times 10^{-4}$ ; however, target F2 is misidentified. These results suggest an optimal  $\theta_{ID}$  that minimizes FAR while maintaining identification performance.

To gain some insight into identification, we can study target F4b (red nylon) as the ID threshold is increased. The primary and local background pixel spectra are shown in Fig. 9(a). The target cannot be fully resolved at this spatial resolution since the

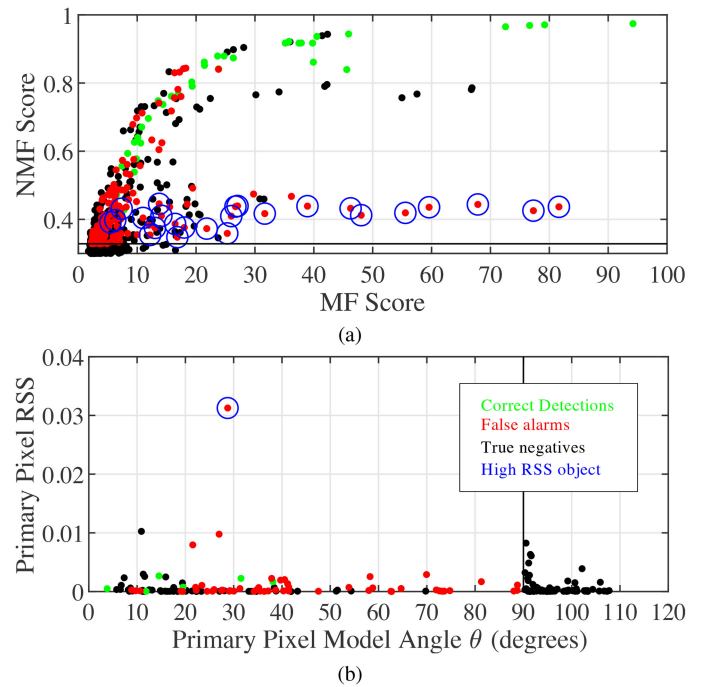


Fig. 10. (a) MF versus the NMF scores are shown for pixels above the initial  $3\sigma$  detection threshold (black). Correct detections, false alarms, and true negatives are shown after ID/FAM processing. (b) Model angles versus RSS are shown for the primary pixels of each object. The blue circle indicates a particular false alarm object with a high MF score but large model error. The 90 model angle threshold is shown in black.

target size (2 m) is smaller than the pixel area (3 m). As a result, the pixel spectrum closely resembles the background. When  $\theta_{ID}$  is increased to 8.5 degrees, target F4b is no longer identified with its truth signature; however, it is identified with another signature for red nylon from the USGS library. Both the true F4 and USGS red nylon signatures are shown in Fig. 9(b) and they are almost identical. The target component  $\hat{t}$  of the model is also shown with estimated model parameters  $\hat{a}_t = 0.01$  and  $\hat{a}_b = [0.54 \ 0.47]^T$ . The small target abundance may be explained by a combination of adjacency effects from the local background and the ground beneath the target. Since the abundance is small, the residual error in the model is evident in the estimated target component.

Increasing  $\theta_{ID}$  further, the target F4b is misidentified as potassium ferrocyanide at  $\theta_{ID} = 17.4$  degrees. From Fig. 9(b), the spectrum of potassium ferrocyanide is very similar to red nylon (7.7 degrees). Apparently, the residual error present in the target estimate is enough to misidentify it as potassium ferrocyanide. This illustrates that as we increase  $\theta_{ID}$  and test more candidate signatures, we increase the possibility of misidentification due to mismatch between library and in-scene spectra.

Fig. 10(a) shows a scatter plot of the NMF versus MF scores for pixels scoring above the initial NMF threshold. The optimal threshold seems to be in the range of 8.5–9.8 degrees. An ID threshold of  $\theta_{ID} = 8.5$  is used, for which each of the targets is correctly identified. After our ID/FAM processing, correct detections are shown in green, false alarms are shown in red, and nontarget (true negative) pixels are shown in black. The initial detection threshold is shown as a solid black line. The ID/FAM



processing removes nontarget pixels that score high on both the NMF and MF. These false alarms could not be eliminated by setting multiple detector thresholds, as suggested in [6], [7].

#### D. Discussion

Although ID/FAM processing significantly reduces the initial number of false alarms, some still remain. As such, an analyst may intervene and assess the confidence of identifications. The model error and estimated target component fit are needed to evaluate the confidence of identification. Pixels containing targets should have small angles between the target component and library signature and small model RSS. These values can be reported along with the identified pixels. As an example, the blue circled pixels in Fig. 10(a) all belong to the same object. These pixels passed the initial NMF threshold and were identified as targets after ID/FAM processing. From Fig. 10(b), however, the object has significantly larger RSS than the other identified pixels and can be removed by setting a threshold on RSS. Large RSS may also indicate the presence of materials not in the library. Objects with low model error, but model angle greater than 90 degrees, have been removed. The estimated target components for these objects are approximately orthogonal to the library signatures and likely due to noise. For this scene, an angle threshold may be set as low as 45 degrees while retaining the targets. Optimal choices for RSS and angle thresholds is a subject of future work.

The ID cluster threshold influences ID/FAM performance. It is important to develop a method to choose  $\theta_{ID}$  to effectively apply ID/FAM. The optimal threshold seems to be in the range of 8.5–9.8 degrees. Based on Fig. 7(b), this is the range of  $\theta_{ID}$  just prior to the number of mixed clusters reaching a maximum. From Fig. 7(c), it is also the range where the number of ID candidates significantly increases (from 8 to 161 signatures). This increases the potential of identifying nontarget materials from the library. As  $\theta_{ID}$  increases further, the number of mixed clusters begins to decrease. The total number of candidates increases, which increases computation cost and deteriorates ID performance. Our results suggest that a good  $\theta_{ID}$  can be selected by first creating plots [Fig. 7(b) and (c)] for the library. The threshold  $\theta_{ID}$  can be chosen such that a significant number of candidates are considered without maximizing the number of mixed clusters. Threshold selection is a complex and challenging task that requires more high-quality data sets to verify results and is a subject of future work.

The computational cost increases with  $\theta_{ID}$ . Since the number of signatures in each cluster increases, there are more candidate spectra to test for each detection. The number of candidate spectra considered at each ID threshold is listed in Table II. The average computation time to model a detected object with a single candidate spectrum on a laptop with a 3.1 GHz Intel Core i7 processor and 16 GB was 5 ms. Processing the whole scene is fast, even when considering hundreds of candidates. The USGS library is modest in size; however, spectral libraries may contain tens of thousands of signatures in practice. The computational savings using the clustered library versus the entire library are significant.

## VI. CONCLUSION

In this article, we propose an efficient processing technique for detecting and identifying materials with large spectral libraries. The proposed technique includes grouping spectrally similar materials within the library for detection and identification. Identification is done by modeling each detected object as a linear mixture between local background and spectrally similar candidate library spectra. The best library model is identified, which automatically removes false alarms. The efficient detection, identification, and false alarm performance for subpixel targets was demonstrated on real hyperspectral data. Optimal dendrogram threshold selection is the subject of future work.

## ACKNOWLEDGMENT

The opinions, interpretations, conclusions, and recommendations presented in this article are those of the authors and are not necessarily endorsed by the U.S. Government.

## REFERENCES

- [1] D. Manolakis, E. Truslow, M. Pieper, T. Cooley, and M. Brueggeman, "Detection algorithms in hyperspectral imaging systems: An overview of practical algorithms," *IEEE Signal Process. Mag.*, vol. 31, no. 1, pp. 24–33, Jan. 2014.
- [2] D. Manolakis, M. Pieper, E. Truslow, T. Cooley, M. Brueggeman, and S. Lipson, "The remarkable success of adaptive cosine estimator in hyperspectral target detection," in *Proc. SPIE 8743, Algo. Technol. Multispectral, Hyperspectral, Ultraspectral Imagery XIX*, May 18, 2013, p. 874302, doi: [10.1117/12.2015392](https://doi.org/10.1117/12.2015392).
- [3] M. T. Eismann, J. Meola, and A. D. Stocker, "Automated hyperspectral target detection and change detection from an airborne platform: Progress and challenges," in *Proc. IEEE Int. Geosci. Remote Sens. Symp.*, 2010, pp. 4354–4357.
- [4] N. M. Nasrabadi, "Hyperspectral target detection: An overview of current and future challenges," *IEEE Signal Process. Mag.*, vol. 31, no. 1, pp. 34–44, Jan. 2014.
- [5] J. Theiler, "Formulation for min–max clairvoyant fusion based on monotonic recalibration of statistics," *Opt. Eng.*, vol. 51, no. 11, 2012, Art. no. 111714.
- [6] R. S. DiPietro, D. Manolakis, R. B. Lockwood, T. Cooley, and J. Jacobson, "Hyperspectral matched filter with false-alarm mitigation," *Opt. Eng.*, vol. 51, no. 1, pp. 1–8, 2012, doi: [10.1117/1.OE.51.1.016202](https://doi.org/10.1117/1.OE.51.1.016202).
- [7] M. Pieper, D. Manolakis, E. Truslow, T. Cooley, and M. Brueggeman, "False alarm mitigation techniques for hyperspectral target detection," in *Proc. SPIE 8743, Algo. Technol. Multispectral, Hyperspectral, Ultraspectral Imagery XIX*, May 18, 2013, p. 874304, doi: [10.1117/12.2015906](https://doi.org/10.1117/12.2015906).
- [8] B. Basener, "An automated method for identification and ranking of hyperspectral target detections," in *Proc. SPIE 8048, Algo. Technol. Multispectral, Hyperspectral, Ultraspectral Imagery XVII*, May 20, 2011, p. 80480D, doi: [10.1117/12.885507](https://doi.org/10.1117/12.885507).
- [9] W. F. Basener, "Ensemble learning and model averaging for material identification in hyperspectral imagery," in *Proc. SPIE 10198, Algo. Technol. Multispectral, Hyperspectral, Ultraspectral Imagery XXIII*, May 5, 2017, doi: [10.1117/12.2263693](https://doi.org/10.1117/12.2263693).
- [10] N. Keshava, "Distance metrics and band selection in hyperspectral processing with applications to material identification and spectral libraries," *IEEE Trans. Geosci. Remote Sens.*, vol. 42, no. 7, pp. 1552–1565, Jul. 2004.
- [11] E. Hirsch and E. Agassi, "Detection of gaseous plumes in ir hyperspectral images using hierarchical clustering," *Appl. Opt.*, vol. 46, no. 25, pp. 6368–6374, 2007.
- [12] S. Lee and M. M. Crawford, "Hierarchical clustering approach for unsupervised image classification of hyperspectral data," in *Proc. IEEE Int. Geosci. Remote Sens. Symp.*, 2004, pp. 941–944.
- [13] N. Gillis, D. Kuang, and H. Park, "Hierarchical clustering of hyperspectral images using rank-two nonnegative matrix factorization," *IEEE Trans. Geosci. Remote Sens.*, vol. 53, no. 4, pp. 2066–2078, Apr. 2015.

- [14] N. Kumar *et al.*, "Hyperspectral tissue image segmentation using semi-supervised NMF and hierarchical clustering," *IEEE Trans. Med. Imag.*, vol. 38, no. 5, pp. 1304–1313, May 2018.
- [15] F. Murtagh, "A survey of recent advances in hierarchical clustering algorithms," *Comput. J.*, vol. 26, no. 4, pp. 354–359, 1983.
- [16] R. F. Kokaly *et al.*, "USGS spectral library version 7," US Geological Survey, Tech. Rep., 2017.
- [17] R. Xu and D. Wunsch, *Clustering*. vol. 10, Wiley, 2008.
- [18] E. Truslow, D. Manolakis, M. Pieper, T. Cooley, and M. Brueggeman, "Performance prediction of matched filter and adaptive cosine estimator hyperspectral target detectors," *IEEE J. Sel. Topics Appl. Earth Observ. Remote Sens.*, vol. 7, no. 6, pp. 2337–2350, Jun. 2013.
- [19] C. Loughlin, E. Truslow, D. Manolakis, A. Weisner, and R. Bostick, "Performance prediction of hyperspectral target detection algorithms via importance sampling," *IEEE J. Sel. Topics Appl. Earth Observ. Remote Sens.*, vol. 12, no. 8, pp. 3078–3091, Aug. 2019.
- [20] C. L. Lawson and R. J. Hanson, *Solving Least Squares Problems*. SIAM, 1995, vol. 15, doi: [10.1137/1.9781611971217](https://doi.org/10.1137/1.9781611971217).
- [21] D. Snyder, J. Kerekes, I. Fairweather, R. Crabtree, J. Shive, and S. Hager, "Development of a web-based application to evaluate target finding algorithms," in *Proc. IEEE Int. Geosci. Remote Sens. Symp.*, Boston, MA, USA, 2008, pp. II-915–II-918, doi: [10.1109/IGARSS.2008.4779144](https://doi.org/10.1109/IGARSS.2008.4779144).



**Cooper Loughlin** received the B.S. degree in electrical engineering from Tufts University, Medford, MA, USA, in 2015, and the M.S. degree in electrical engineering from Northeastern University, Boston, MA, USA, in 2018. He is currently working toward the Ph.D. degree at Northeastern University.

He is also currently a Research Assistant with MIT Lincoln Laboratory, Lexington, MA, USA. His research interests include hyperspectral imaging, digital signal processing, and machine learning.



**Michael Pieper** received the B.S. and M.S. degrees in electrical engineering from Northeastern University, Boston, MA, USA, in 2007, and the Ph.D. degree in electrical engineering from the Northeastern University, in 2017.

He is currently a Technical Staff Member with MIT Lincoln Laboratory, Lexington, MA, USA. His research interests include atmospheric compensation, detection, identification, and temperature-emissivity separation in hyperspectral imaging remote sensing.



**Dimitris Manolakis** received the B.S. degree in physics and the Ph.D. degree in electrical engineering from the University of Athens, Greece, in 1976 and 1981, respectively.

He is currently a Senior Staff Member with the Massachusetts Institute of Technology (MIT), Lincoln Laboratory, Lexington, MA, USA. He is a coauthor of the textbooks *Digital Signal Processing: Principles, Algorithms, and Applications* (Prentice Hall, 2006, 4th ed.), *Statistical and Adaptive Signal Processing* (Artech House, 2005), *Applied Digital*

*Signal Processing* (Cambridge University Press, 2011), and *Hyperspectral Imaging Remote Sensing* (Cambridge University Press, 2016).

**Andrew Weisner** received the B.S. and M.S. degrees in chemistry from Wright State University, Dayton, OH, USA, in 2001 and 2003, respectively.

He is a Chemist working in the field of spectral data exploitation with the U.S. Air Force National Air and Space Intelligence Center, Wright-Patterson AFB, OH, USA.

**Randall Bostick** received the B.S. degree in mathematics and the M.S. degree in physics from Wright State University, Dayton, OH, USA, in 1990 and 1997, respectively, and the Ph.D. degree in electro optical sciences from the Air Force Institute of Technology, Wright-Patterson AFB, OH, USA, in 2013.

He is an Image Scientist working in the field of spectral data exploitation with the U.S. Air Force National Air and Space Intelligence Center, Wright-Patterson AFB.



**Thomas Cooley** received the B.S. degree in electrical engineering from Rensselaer Polytechnic Institute, Troy, NY, USA, in 1988, the M.S. degree in electrical engineering and applied physics from the California Institute of Technology (Caltech), Pasadena, CA, USA, in 1991, and the Ph.D. degree in optical sciences from the University of Arizona/Tucson, AZ, USA, in 1995.

He is the Chief Scientist, Space Vehicles Directorate, Air Force Research Laboratory, Air Force Materiel Command, Kirtland Air Force Base, Albuquerque, NM, USA. He was the Principal Investigator of the Artemis payload, a hyperspectral sensor to demonstrate the use of this rich data source for the wide range of applications, and the Program Manager for the TacSat-3 Satellite launched in May 2009. He is a coauthor of the textbook *Hyperspectral Imaging Remote Sensing* (Cambridge University Press, 2016).

Dr. Cooley is a member of the scientific and technical cadre of senior executives, Kirtland Air Force Base.